



# Polarization retention and switching in ferroelectric nanocapacitors with defects on tensile substrates

I.B. Misirlioglu\*, M. Yildiz

Faculty of Engineering and Natural Sciences, Sabanci University, Tuzla/Orhanli, 34956 Istanbul, Turkey

## ARTICLE INFO

### Article history:

Received 4 April 2011

Received in revised form 25 July 2011

Accepted 8 August 2011

Available online 13 September 2011

The review of this paper was arranged by Dr. Y. Kuk

### Keywords:

Ferroelectric thin film devices

Domains

Hysteresis

Thermodynamic modeling

## ABSTRACT

We analyze the effect of defects on the polarization stability and switching of epitaxial nanocapacitor ferroelectric films on tensile substrates using a thermodynamic approach. Defects are either frozen-in dipoles of the *p*-type or trapped space charges. The retention of the in-plane ferroelectric polarization does not suffer nearly at all from the possible presence of dead layers or polar defects but is dramatically impacted by relatively high densities of space charge. Switching is a strong function of defects as well as the presence of a bottom electrode. The out-of-plane dielectric displacement exhibits a spike during switching of the in-plane polarization in films with bottom electrodes but nearly disappears otherwise. Such an effect during polarization reorientation along the film plane could be tailored as a sensing signal. The hysteresis and domain characteristics as a function of interface conditions and defects are discussed for BaTiO<sub>3</sub> strained on tensile substrates.

© 2011 Elsevier Ltd. All rights reserved.

## 1. Introduction

Long term stability of a switchable ferroelectric polarization (*P*) in epitaxial thin films have been a topic of interest for many research groups as well as the integrated circuit (IC) industry. The designs employing a ferroelectric polarization in a capacitor-type structure have mostly focused on systems with the ferroelectric being sandwiched between two electrodes through which the data or agent signal can both be generated and sensed. It is now well known that ferroelectrics in thin film form sandwiched between two metallic electrodes can suffer from the formation of an utterly non-ferroelectric, insulating layer at the film-electrode interface [1–12] in addition to spatial defect fields such as that of the dislocation type [13–15]. Very recently, the polarity of the interfaces have come to the attention of Wang et al. as a possible effective mechanism determining the limit to ferroelectric behavior [16]. Moreover, migration of ionic species under fields emanating from inhomogeneities, especially oxygen vacancies, towards domain–domain and metal–film interfaces contribute to the ferroelectric stability [17–19].

While the sandwich type capacitor (SC) is the most famous the geometry studied, the polarization stability in interdigitated finger electrode type capacitors (IFEC) have attracted some limited attention of a few groups [20–26], including a study on electrode geometry effects [27]. IFECs have mostly been on the agenda for tunable

device applications. At a first glance, what appears to be promising for such finger electrode ferroelectric capacitor systems as potential memory elements is that an in-plane *P* might not suffer from any depolarizing effects originating from the condition that  $\nabla \cdot D = 0$  at interfaces with passive layers. Therefore, a switchable *P* that is minimally impacted by the film–electrode interface conditions might be feasible to tailor. Furthermore, in case of diffusion of ionic species and vacancies under cyclic applied fields, the potential drops driving such formations along the film plane occur at larger distances, meaning that a longer-lasting benefit from the ferroelectric *P* might be realized. Despite all these, remanence of *P* and the transition characteristics of FE films with interdigitated finger electrodes remains as a topic studied in a very limited number of works.

In this article, we study the electrical properties of [001] BaTiO<sub>3</sub> (BT) grown on epitaxially tensile perovskite type [001] single crystal substrates (TSC) to quantitatively study the effect of IFEC electrostatic boundary conditions on *P* configurations. Compressive substrates for BT usually favors an out-of-plane *P* while TSC induces an in-plane *P* owing to the tensile misfit with BT. Employing the Landau–Ginzburg–Devonshire (LGD) functional in a two dimensional frame, we compare and contrast on the differences of properties for the two capacitor geometries with dead layers at the film–electrode interfaces. We find that frozen-in defect complexes due to ionic vacancies do not so profoundly alter the IFEC films in contrast to SC type capacitors. Moreover, we also find that the BT films in the IFECs exhibit a “spike” of dielectric displacement at the exposed surface between the electrodes and that this

\* Corresponding author. Tel.: +90 216 4839562; fax: +90 216 4839550.  
E-mail address: [burc@sabanciuniv.edu](mailto:burc@sabanciuniv.edu) (I.B. Misirlioglu).

behavior is a very strong function of whether a bottom electrode is present or not. The presence of such an effect can be tailored as an effective means to sense in-plane  $P$  switching.

## 2. Theory and methodology

The schematic of the capacitor geometry considered is given in Fig. 1. A two dimensional grid is constructed that has  $400n \times kn$  cells where  $k$  (400) is the number of cells along the film thickness (width) and each cell,  $n$ , has a dimension of 0.4 nm, nearly the lattice parameters of well known pseudocubic perovskites such as BT to imitate the order of lengths at which  $P$  can vary.

$P$  is obtained by solving the equations of state derived from the LGD free energy for an epitaxial monodomain (001) ferroelectric film on a (001) cubic substrate coupled with the Maxwell equation for dielectric displacement employing a finite difference discretization. The total volumetric free energy of the ferroelectric thin film capacitor system is:

$$F_T = \int_V [w(F_0 + F_P + F_E + F_G - F_{ES}) + (1-w)F_{DL}]dV \quad (1)$$

where  $w$  is a step-wise function defining the interface between the dead layer and the ferroelectric:  $w = 1$  when  $-h/2 \leq z \leq +h/2$  and  $w = 0$  when  $-h/2 - s < z < -h/2$  and  $+h/2 < z < s + h/2$ ,  $s$  is the dead layer thickness (one unit cell in this work when present, zero when absent),  $h$  is the thickness of the ferroelectric layer. The electrode-dead layer interfaces are at  $-h/2 - s$  and  $s + h/2$  respectively.  $F_0$  is the energy of the paraelectric state and is taken as zero due to the absence of order-parameter related terms.  $F_P$  is the energy due to the presence of  $P$  and is given by

$$F_P = \alpha_1(P_1^2 + P_2^2 + P_3^2) + \alpha_{11}(P_1^4 + P_2^4 + P_3^4) + \alpha_{12}(P_1^2P_2^2 + P_1^2P_3^2 + P_2^2P_3^2) + \alpha_{111}(P_1^6 + P_2^6 + P_3^6) + \alpha_{112}[P_1^4(P_2^2 + P_3^2) + P_2^4(P_1^2 + P_3^2) + P_3^4(P_1^2 + P_2^2)] + \alpha_{123}P_1^2P_2^2P_3^2 \quad (2)$$

where  $P_i$  ( $i = 1,2,3$ ) are the components of  $P$  in the ferroelectric state, and  $\alpha_i$ ,  $\alpha_{ij}$ , and  $\alpha_{ijk}$  are the dielectric stiffness coefficients.  $F_E$  in Eq. (1) is the internal elastic energy both due to the misfit between

the film and the substrate,  $\varepsilon_{ij}$  as well as the self-strain in the ferroelectric state,  $\varepsilon_{ij}^0$ , given by:

$$F_E = \frac{1}{2}C_{ijkl}(\varepsilon_{ij} - \varepsilon_{ij}^0)(\varepsilon_{kl} - \varepsilon_{kl}^0) \quad (3)$$

where the  $C_{ijkl}$  are the elastic stiffnesses for a cubic crystal.  $\varepsilon_{ij}^0$  is the transformation strain due to the paraelectric–ferroelectric phase transition in the film and is given by:

$$\varepsilon_{ij}^0 = Q_{ijk}P_k \quad (4)$$

with  $Q_{ijk}$  being the electrostrictive coefficient tensor for a cubic crystal. The shear components of misfit stress in (3) are taken as zero due to the traction-free film surface. The in-plane biaxial misfit state with equal orthogonal components  $\varepsilon_{11} = \varepsilon_{22}$ , due to epitaxy require that  $P_1 = P_2$ , and the rest of the equations are given hereafter accordingly. The gradient energy in Eq. (1) we employ is:

$$F_G = G_{33}\left(\frac{dP_3}{dz}\right)^2 + G_{31}\left(\frac{dP_3}{dx}\right)^2 + G_{13}\left(\frac{dP_1}{dz}\right)^2 + G_{11}\left(\frac{dP_1}{dx}\right)^2 + G_{23}\left(\frac{dP_2}{dz}\right)^2 + G_{21}\left(\frac{dP_2}{dx}\right)^2 \quad (5)$$

where  $G_{ij}$  are the gradient energy coefficients. For the sake of convenience, we shall assume that the gradient energy coefficient is isotropic,  $G_{33} = G_{31} = G_{13} = G_{11} = G_{23} = G_{21} = G$ .  $F_{ES}$  is the electrostatic energy of the system that is a function of the electrostatic boundary conditions of the capacitors as well as gradients of  $P$  and can simply be written as:

$$F_{ES} = -(E_xP_1 + E_zP_3) \quad (6)$$

for  $w = 1$  where  $E_x$  and  $E_z$  are the in-plane and out-of-plane components of the electric field respectively.  $F_{DL}$  is simply the energy of the dead layer that is assumed to be a linear dielectric and is given by (for  $w = 0$ ):

$$F_{DL} = \varepsilon_0\varepsilon_r(E_x^2 + E_z^2) \quad (7)$$

where  $\varepsilon_r$  is the dielectric constant of the dead layer and is assumed to be isotropic for convenience. Minimization of Eq. (1) for  $w = 1$  yields the Euler–Lagrange relations as:

$$\begin{aligned} \frac{dF_T}{dP_3} - \frac{d}{dz}\left(\frac{dF_T}{df_1}\right) - \frac{d}{dx}\left(\frac{dF_T}{df_2}\right) &= 0, \\ \frac{dF_T}{dP_1} - \frac{d}{dz}\left(\frac{dF_T}{df_3}\right) - \frac{d}{dx}\left(\frac{dF_T}{df_4}\right) &= 0 \end{aligned} \quad (8)$$

with  $f_1 = dP_3/dz$ ,  $f_2 = dP_3/dx$ ,  $f_3 = dP_1/dz$  and  $f_4 = dP_1/dx$ . From Eqs. (8) and (1), the equations of state for the ferroelectric layer are written as:

$$\begin{aligned} G\left(\frac{d^2P_3}{dz^2} + \frac{d^2P_3}{dx^2}\right) &= 2\alpha_3^mP_3 + 4\alpha_{13}^mP_3P_1^2 + 4\alpha_{33}^mP_3^3 + 6\alpha_{111}P_3^5 \\ &+ \alpha_{112}(4P_3P_1^4 + 8P_3^3P_1^2) + 2\alpha_{123}P_3P_1^4 \\ &- E_z(x,z) \end{aligned} \quad (9a)$$

$$\begin{aligned} G\left(\frac{d^2P_1}{dz^2} + \frac{d^2P_1}{dx^2}\right) &= 2\alpha_1^mP_1 + 2(2\alpha_{11}^m + \alpha_{12}^m)P_1^3 + 2\alpha_{13}^mP_1P_3^2 \\ &+ 6\alpha_{111}P_1^5 + 2\alpha_{112}[3P_1^5 + 3P_1^3P_3^2 + P_1P_3^4] \\ &+ 2\alpha_{123}P_1^3P_3^2 - E_x(x,z) \end{aligned} \quad (9b)$$

in the ferroelectric film ( $w = 1$ ) where the  $\alpha_3^m$ ,  $\alpha_{13}^m$ ,  $\alpha_{33}^m$  are the renormalized dielectric stiffness coefficients, modified by the misfit strain and the two-dimensional clamping of the film [28]. The dead layer, when present, is assumed to be a high- $k$  dielectric whose dielectric constant,  $\varepsilon_r$ , is 20 to exemplify its effects. The electric

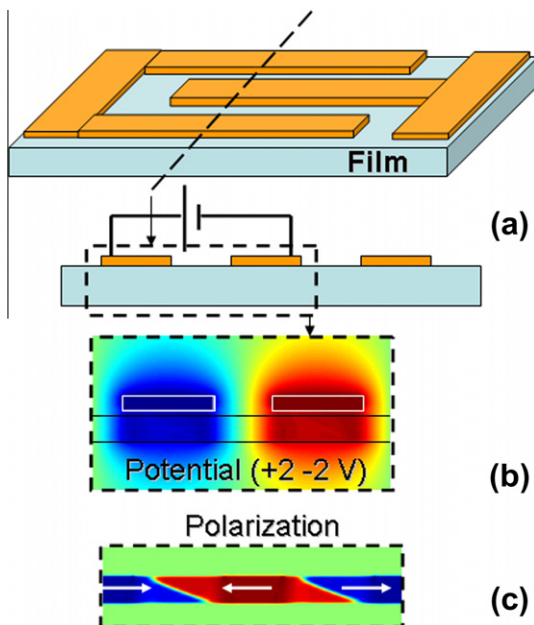


Fig. 1. (a) A schematic of the finger electrode capacitor. The potential in (b) and the in-plane polarization components in (c) are shown for demonstrative purposes.

fields in both the ferroelectric layer and the dead layer are computed from the gradient of the electrostatic potential  $\phi$ ,

$$E_z = -\frac{d\phi}{dz}, E_x = -\frac{d\phi}{dx} \quad (10)$$

Note that  $\phi$  contains all contributions from boundaries, defects and charge distributions when present and is solved at each point in the system as a function of  $P$  components from the Maxwell relation  $\text{div}D = \rho$  that can explicitly be written as,

$$\frac{d^2\phi}{dz^2} + \frac{d^2\phi}{dx^2} = \frac{1}{\epsilon_b\epsilon_0} \left( \frac{dP_z}{dz} + \frac{dP_x}{dx} - \rho \right) \quad (11a)$$

in the ferroelectric layer and

$$\frac{d^2\phi}{dz^2} + \frac{d^2\phi}{dx^2} = \frac{\rho}{\epsilon_r\epsilon_0} \quad (11b)$$

in the dead layer where  $\rho$  is the volumetric charge density (0 when no impurities are present) with  $\epsilon_b$  being the background dielectric constant of the ferroelectric (taken as 10 in this work). The boundary conditions we employed for  $P_{1,3}$  are

$$\left[ P_1 + \lambda \frac{dP_1}{dz} \right]_{z=-\frac{h}{2}-s, \frac{h}{2}+s} = 0, \left[ P_3 + \lambda \frac{dP_3}{dz} \right]_{z=-\frac{h}{2}-s, \frac{h}{2}+s} = 0 \quad (12)$$

at the top and bottom electrode-film interface of the ferroelectric where the extrapolation length,  $\lambda$ , is taken as infinite. Periodic boundary conditions are used along the  $x$ -axis, i. e.,  $P_3(z, x=0) = P_3(z, x=L)$ ,  $P_1(z, x=0) = P_1(z, x=L)$ . We apply Dirichlet boundary conditions to solve the electrostatic potential. At the dead layer-electrode interfaces  $-h/2 - s$  and  $s + h/2$ ,  $\phi = 0$  correspond to total charge compensation while periodic boundaries are adopted along  $x$  as given above.  $\phi$  is given for the two electrodes as exemplified in Fig. 1b. The free surfaces in the IFEC capacitor has to satisfy Eq. (11) and periodic boundaries are employed along  $x$ . The effect of a bottom electrode in the IFEC system is considered via assigning  $\phi = 0$  @  $z = -h/2 - s$  when specified.

Eqs. 9a, 9b, 10, 11a, 11b, 12 are solved simultaneously employing a Gauss–Seidel iterative scheme subject to boundary conditions mentioned above and (11) and (12) for  $P$ . We limit ourselves to 5000 iterations converging to a difference of about  $10^{-8}$  between consecutive iterative  $P$  solutions when ferroelectricity exists. The defects, when present, are assumed to be frozen-in polar complexes in the lattice with the restriction that they cannot be too close to each other in order to test long-range effects or they are space charges due to ionized impurities ( $\rho \neq 0$ ). For the former case, their presence is introduced via fixing the relevant  $P$  components at a randomly chosen cell, creating local frozen-in dipoles. Thus the impact of the frozen-in type defects is two fold: They can pin local  $P$  via the gradients in  $P$  they create and these gradients also produce a spatially varying potential via Eq. (11a) under given boundary conditions. Thus  $E_{x,z}(x, z)$  in Eqs. (9a) and (9b) contains the defect fields, too, via the spatial gradients of the potential computed from Eq. (10) with the boundary conditions for  $P$  and  $\phi$  in the system.

As prescribed above, the frozen-in dipole defect positions are fixed with respect to the bottom electrode/free surface coordinates. Thus, their positions are automatically altered when film thickness changes. This mostly impacts the symmetry of the defect positions with respect to the midsection of the film for ultrathin films but is still good enough to demonstrate their effects in ultrathin structures. We also must add here that, within the 2D limit of the study, our results for IFECs with defects might not be exactly representing the behavior of 3D systems with very few defects due to variation in the averaging of properties. On the other hand, they can be compared to 3D systems with relatively high density of

defects where averaging over the volume will be close to the averaging over a 2D slice of the system considered here.

To get the electric field dependent behavior of the films, we simply change  $\phi$  on the left electrode, assigning the other  $-\phi$ . A triangular signal for  $\phi$  is used to get the hystereses of the films with maximum voltage drop amplitude being 4 V. The signal consists of 100 steps between  $-2$  V and  $+2$  V and each electrode attains the opposite sign of the other. Note that the fields will be highly inhomogeneous in the IFEC. At every incremental bias step, we allow the films to reach their near-equilibrium  $P$  configuration. Hence, the hystereses in our simulations are in the quasi static limit. The electrode thicknesses are 8 nm and due to the free surfaces exposed between the top electrodes, we solve the  $\phi$  outside the IFEC films, too. The section exposed between the array of finger electrodes is 32 nm. These IFEC films also experience fields between the finger electrodes and a grounded bottom electrode when there is one. Fig. 1b–c is an example to demonstrate the characteristic distribution of potential and the  $P_x$  under 2 V bias between the finger electrodes.

We considered in this study the heteroepitaxial (001) BT films fully strained on a non-ferroelectric (001) hypothetical cubic perovskite substrates inducing a 1% tensile misfit with interdigitated metallic finger electrodes (IFEC). We assumed this hypothetical substrate for demonstrative purposes. However, the approach presented here can easily be adapted to any pseudocubic ferroelectric perovskite film. The values of the dielectric stiffness coefficients and other thermodynamic parameters of BT entering the calculations are taken from Ref. [22]. Simulation results are presented for films of 8 nm, 16 nm thickness at room temperature ( $T = 25^\circ\text{C}$ ).

### 3. Results and discussion

Here we discuss the results for the ferroelectric IFEC films at RT, under a fixed applied bias as well as a triangular signal. We consider dipolar defects whose schematic is given in Fig. 2: A frozen-in, dipole couple or so-called  $p$ -type complex formed due to a missing O vacancy where the B-site ions are shifted into opposite corners in the two neighboring unitcells to reduce repulsive forces under fully ionic consideration. The variants of this type of defect in this work is chosen randomly and therefore the defect dipole moment can point along any of the 2 axes given in Fig. 2.

Such a defect constitutes a so-called  $p$ -type defect [29] and is similar to the defect type whose mechanism of formation was reported in Ref. [30] accompanied by relaxation of the atomic forces.

Due to the different variations in electrostatic potential around the types of defects mentioned above, they might be expected to

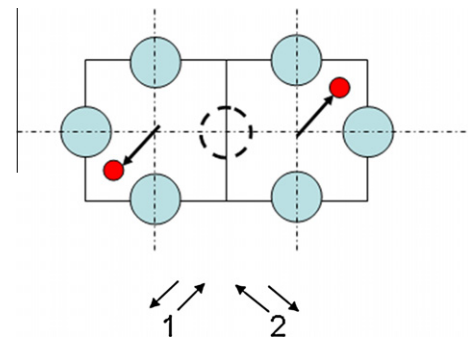


**Fig. 2.** The  $p$ -type defects in this study. The dashed circle in the middle denotes the missing oxygen ion while the red atoms denote the Ti ions. The arrows indicate the shift of the positively charged Ti ions, forming an antiparallel configured dipole couple of not-ferroelectric origin. 1 and 2 denote the possible configurations considered in this work.

have a quite complicated impact on the properties of IFEC films. Atomistic first principles studies have reported substantially high dipole moments for vacancy-induced dipoles, comparable to or more than the moments of spontaneous ferroelectric dipoles [31]. Keeping in mind the results of these studies, we consider highly stable defect-dipole sites whose values are assigned as  $0.25 \text{ C/m}^3$ , close to the bulk  $\text{BaTiO}_3$   $P$  at RT. In Section 3.2., we also give our results for domain structures of  $P$  in IFEC films in the presence of homogeneous space charge distribution as the trends for remanence we observed are quite different than polar defects.

### 3.1. Ferroelectricity at room temperature in IFEC thin film capacitors

Using exactly the same method described in Section 2 with the appropriate BCs, we provide our RT results for the IFEC films in this section. During the simulations of the domain states in the IFEC films, we note that the presence or absence of a dead layer ( $s = 0$  or  $s = 1$  respectively) has no significant impact on the domain morphologies of the 8 nm and 16 nm thick IFEC films with or without defects. Therefore we give in this section our results for  $s = 1$  to avoid repetition of similar plots and evaluation. We emphasize here the states under bias (sufficient to saturate the  $P_x$  in the plane of the film) followed by removal of the bias. The latter is to display the domain configuration under remanence. We consider IFEC films only with top finger electrodes throughout the discussion. For the RT results herein presented, the presence of a bottom electrode also has no apparent influence on the  $P$  configuration near saturation bias followed by zero bias. The effect of a bottom electrode, however, becomes a very important parameter for switching where related details are discussed in Section 3.4.

Solution of the  $P_x$  and  $P_z$  starting from fluctuations around zero under 1% tensile misfit at zero bias develop into a single domain state of remanent  $P_x$  pointing in either  $-x$  or  $+x$  direction with zero  $P_z$  and these are not given here for brevity. Applying 1.5 V and  $-1.5 \text{ V}$  bias on the electrodes respectively, we show in Fig. 3a–c the in-plane domain state stability of  $P_x$  in the 8 and 16 nm thick defect-free films. The resultant configuration is the consequence of the inhomogeneous distribution of the field inside the film. Field distribution in finger electrode capacitors have been often approximated as a constant in-plane field, which is a very unrealistic assumption that would prevent correct evaluation of such systems.

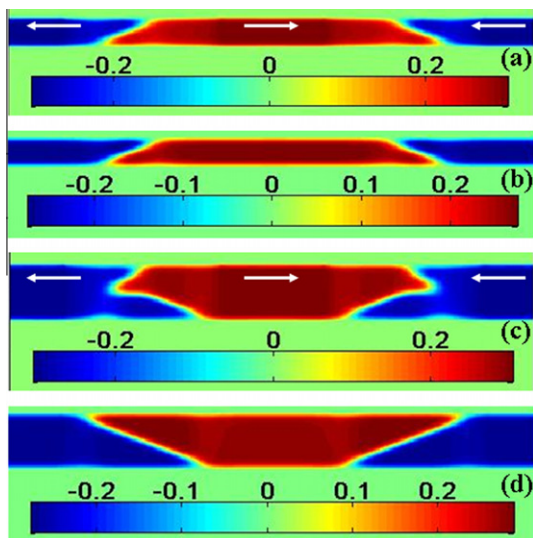


**Fig. 3.** Map of  $P_x$  in (a) 8 nm thick defect-free IFEC film under bias, (b) 8 nm thick defect-free IFEC film after bias removed, (c) 16 nm thick defect-free IFEC film under bias, (d) 16 nm thick defect-free IFEC film after bias removed.

In agreement with our conclusions, Ref. [25] shows that this highly inhomogeneous distribution even in larger real systems lead to different retention and fatigue behavior of in-plane  $P$  in different regions with respect to the electrode positions. Likewise, in this study, removal of the bias leads to an apparently stable remanence of  $P_x$  that changes sign along  $x$  both in the 8 nm and 16 nm thick films as displayed in Fig. 3b–d.

Due to the condition of the remanent  $P$  being parallel to the interface, there is no jump in dielectric displacement at neither  $z = h/2$  or  $z = -h/2$ , hence no depolarizing fields along  $x$  when external bias is zero. Therefore the 8 nm and 16 nm IFEC films do not suffer much from thickness effects compared to the SC ones.  $P_z$  has small but finite values at zero bias near the domain boundaries but attains spatially varying solutions at the order of  $P_x$  under bias due to the potential drops from the finger electrodes towards bottom of the film.

#### 3.1.1. $p$ -type defects present

When the aforementioned type of defects are present with  $s = 1$ , the above picture for the 8 nm film only slightly changes. Turning our attention to Fig. 4a–b for the 8 nm IFEC films with  $p$ -type defects, we see no induction of any type of nano-sized domains. Upon removal of the bias, the  $P_x$  configuration does not change much and more or less sustains its state in the biased case for  $p$ -type defects (Fig. 4b). The domain boundaries between the  $P_x$  components pointing along  $-x$  and  $+x$  directions undergoes a slight or even negligible rearrangement.  $P_z$ , after removal of the bias, is zero except components forming due to slight rotations of  $P$  near the interfaces where  $P_x$  changes sign.

Therefore, we observe from Fig. 4 that, even in the presence of dipolar defects, there is hardly any loss of the spatial state in between the electrodes attained under bias. The common observation in the simulations of the IFEC films here is that defects act as local perturbation centers to the order state and do not trigger domain formation. However, these RT results obviously do not imply that the hystereses and phase transition characteristics for the defected and defect-free 8 nm thick IFEC films will also be similar.

Looking at the response of the 16 nm IFEC film with  $p$ -type defects given in Fig. 5, we again see that the configuration of  $P_x$  under bias (Fig. 5a) and zero bias (Fig. 5b) are similar, with the exception of the interface asymmetry with respect to the midpoint of the structure in the 16 nm IFEC with  $p$ -type defects. The same configurational trend of  $P_x$  distribution as in the 8 nm IFEC film is observed but a larger switched volume is present in 16 nm film. Stability of  $P_x$  under applied bias and upon removal of the bias in the IFEC films with defects is only slightly altered.

If examined carefully via Figs. 4 and 5 and 5, the defects near the bottom interface of the 16 nm film are more visible under zero bias and appear to have a larger area of influence in contrast to the 8 nm thick one. This is because of the decay of the magnitude of the electric field into the film volume away from the finger electrodes and that the “defect configured  $P_x$ ” becomes more prominent around defects compared to applied field effects in the 16 nm film. Regions

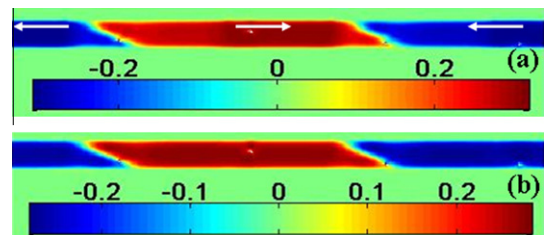


**Fig. 4.** Map of  $P_x$  in (a) 8 nm thick IFEC film with  $p$ -type defects under bias, (b) 8 nm thick IFEC film with  $p$ -type defects after bias removed.

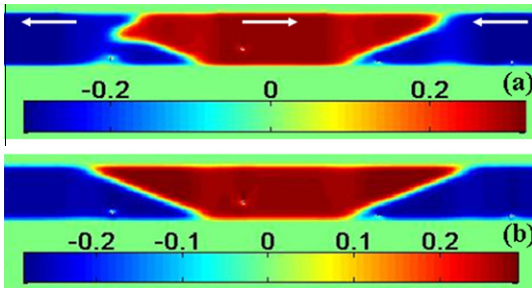


**Fig. 5.** Map of  $P_x$  in (a) 16 nm thick IFEC film with  $p$ -type defects under bias, (b) 16 nm thick IFEC film with  $p$ -type defects after bias removed.

in the vicinity of the electrodes are naturally under a stronger influence of the applied bias and this overrides the effects due to dipolar defects as in the 8 nm thick film. But again it should be borne in mind that the stabilities of the  $P_x$  components shown in the color-map plots do not reveal how the hystereses would be impacted by these defects.

Overall, the  $P_x$  component in the IFEC films under tensile in-plane misfit strains appear to be stable without any electrical domain complications similar to that of observed in the SC films. The remanence mentioned for the IFEC geometry, on the other hand, is the stability of a switchable but a local  $P_x$  with respect to the electrode positions and widths. The electrostatics fields of the  $p$ -type defects is also more complicated as there is an abrupt sign change of  $P_x$  and  $P_z$  at the sites neighboring defected cells. But we did not observe any dramatic variations in the domain configurations of IFEC films with  $p$ -type defects.

### 3.1.2. Space charge formation present

Continuous distribution of space charge due to relatively large densities of carriers trapped at deep states have been mostly analyzed in SC type ferroelectrics and superlattices [32–39]. Such formations can also have a significant impact on the remanence of the  $P_x$  in IFEC capacitors. We give our results here for a constant density and an asymmetrically distributed density of space charge under bias and after removal of bias with no bottom electrode present. Fig. 6a–d displays the state of  $P_x$  under total 4 V bias followed by removal of this bias for the 16 nm and 8 nm thick IFEC films respectively. A continuous distribution of space charge at constant density of  $10^{24}$  C/m<sup>3</sup> does not have an apparent effect on  $P_x$  in both the 16 nm thick IFEC film when under bias and when no bias exists and is skipped here. Such a charge distribution normally produces an electric field in a slab that is zero in the middle and is symmetrical with respect to the mid-section of the film thickness. However, one should pay attention that, in the case of finger electrodes, this situation becomes quite different owing to boundary conditions. When looking at Fig. 6a–b, a homogeneous  $\rho$  of  $10^{26}$  C/m<sup>3</sup>, on the other hand, significantly interferes with the applied field and there is no single domain remanence in the region between the electrodes upon removal of the applied in-plane bias.

A homogeneous space charge density of  $10^{24}$  C/m<sup>3</sup> does not influence the stability of the  $P_x$  in the 8 nm thick IFEC both in the presence and absence of applied, the system retains its “under-bias  $P_x$ ” state and is not given here for brevity. Raising this value to  $10^{26}$  C/m<sup>3</sup>, however, alters  $P_x$  and  $P_z$  dramatically where a periodic domain structure in  $P_x$  that is smaller than the electrode periodicity is obtained upon removal of bias as provided in Fig. 6c and d. We also note that the switched fraction under applied bias in the 8 nm IFEC film is much smaller in relative volume than the charge-free 8 nm thick IFEC already given in Fig. 3a. Upon removal of applied bias, these volumetric charge dictates the state of  $P_x$  and

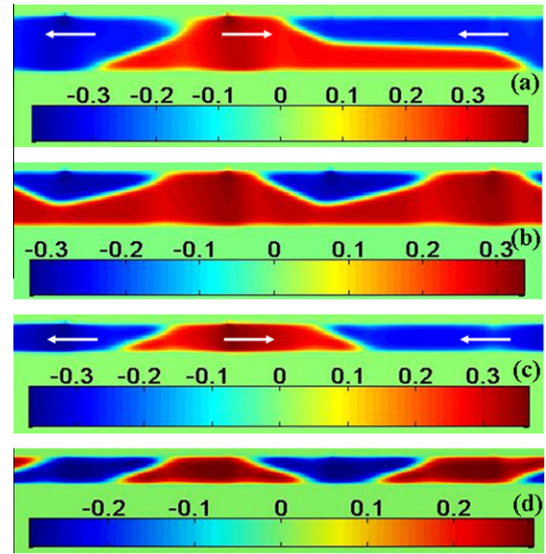


**Fig. 6.** Map of  $P_x$  in (a) 16 nm thick IFEC film with homogeneous space charge density of  $10^{26}$  C/m<sup>3</sup> under 4 V bias and (b) after bias removed, (c)  $P_x$  in 8 nm thick IFEC film with homogeneous space charge density of  $10^{26}$  C/m<sup>3</sup> under bias and (d) after bias removed.

the configuration induced under bias is totally destroyed (Fig. 6c and d).

## 3.2. Characteristics of the hysteresis loops in IFEC films

### 3.2.1. No defects

Applying the triangular bias signal as explained in Section 2, we extracted the hysteresis loops of the IFEC films for  $P_x$ . As already mentioned, the field distribution in this geometry is not uniform along the film volume and that parts of the films switch in opposite directions. The region between the electrodes are tracked to probe the  $P_x$  and  $P_z$  as a function of applied bias signal because the average  $P_x$  of the entire film does not yield a hysteresis due to the inhomogeneous nature of the field distribution in the given electrode positions. Noting that the presence or absence of a dead layer does not make a difference in the IFEC geometry, we studied this system for  $s = 1$ . The very reason for this is that there is no remanent  $P$  component in the dielectric displacement normal to the electrode–film interface. We computed the average dielectric displacement at the surface exposed between the top finger electrodes to identify whether a signal here is possible to tailor during switching of  $P_x$ .

Fig. 7a and b displays the hysteresis loop in the 8 nm and 16 nm thick IFEC films in both the presence and absence of a bottom electrode where  $P_x$  in the middle of the region between the electrodes was tracked. In the absence of defects, there is nearly identical square hystereses in both IFEC films. Also in Fig. 7, the impact of the presence of a bottom electrode in the IFEC films is clear: Both the 8 nm and 16 nm films switch at a lower coercive field in the thermodynamic limit. Moreover, films without the bottom electrodes have a displaced hysteresis towards the positive bias, indicating it is more difficult for  $P_x$  to switch from  $-x$  to  $+x$  direction in the middle region between the electrodes. This difference in the switching behavior in the IFEC films with bottom electrodes is due to the presence of a large out-of-plane electric field formation that stabilizes an induced  $P_z$  coupling to  $P_x$  via the cross terms in the LGD energy. Right at the coercive bias of  $P_x$  we find relatively large values for the solution of  $P_z$  and nearly zero elsewhere in the bias range of interest. Therefore the film with the bottom electrode passes through an “easy induced” monoclinic state during

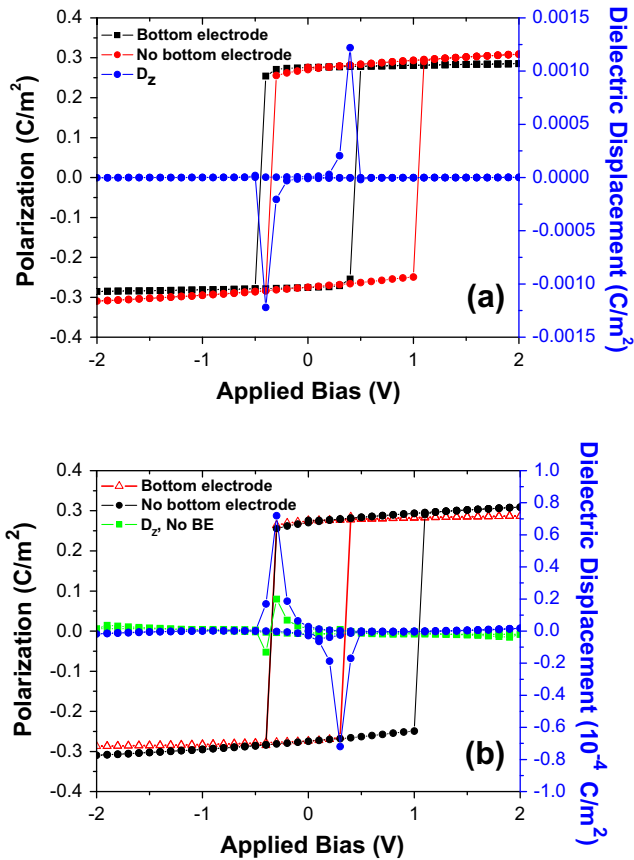


**Fig. 7.** Hysteresis loops and dielectric displacement along  $z$  (right axis) for defect-free (a) 8 nm thick IFEC film and (b) 16 nm thick IFEC film. ‘BE’ (b) stands for ‘bottom electrode’ and the green curve is provided to display the dielectric displacement at the surface between the electrodes when there is no bottom electrode.

switching favored by the field along  $z$  axis which seems to reduce the coercive field value for  $P_x$ .

The thickness dependent effects in IFEC films with dead layers do not have an as profound an effect on remanent  $P$  stability as in SC films. Moreover, this “nearly dead-layer independence of polarization” of IFEC films is a very important and advantageous aspect in device design. We find that  $\langle D_z \rangle$  on the exposed surface between the top-electrodes, especially in the presence of a bottom electrode, undergoes abrupt variations near the coercive bias values of  $P_x$ . These peak-like abrupt variations in  $D_z$  could be useful as a sensing signal of the switching for instance, via tracking the change of dielectric displacement along  $z$  near the bottom electrode or an electrode placed in between the top ones. One important finding is that the sign of these peaks are thickness dependent and, in the absence of the bottom electrode, such peaks nearly disappear and become very weak or negligible. This is because of the depolarizing fields taking effect that oppose  $P_z$  during the switching of the  $P_x$  and thus no clear peak-like  $P_z$  variations are observed. Therefore, the ease with which  $P_z$  switches also impacts the switching characteristics of  $P_x$  as demonstrated.

### 3.2.2. $p$ -type defects present

We now discuss the effect of  $p$ -type type defects on the 8 nm and 16 nm thick IFEC films for  $s = 1$ . In this section, we again skip the discussion of the characteristics of the hystereses for  $s = 0$  because whether  $s = 0$  or  $s = 1$  has only a negligible effect on the behavior of  $P_x$  in the IFEC films. Owing to the highly inhomogeneous fields during hysteresis extraction tracking the  $P_x$  in the

middle section of the film is what we pursue again in order to justify defect related effects.  $P_x$  in the central region between the electrodes is influenced by their existence, even if several tens of nanometers away from defect sites implying the long-range effects of frozen-in dipole complexes. We next discuss the alterations in the hysteresis loops in the 8 nm and 16 nm films with defects.

The presence of  $p$ -type defects have a substantial influence on the hystereses of both the 8 nm and 16 nm thick films as seen in Fig. 8a and b. In the presence of bottom electrodes, there is a visible shift of the hysteresis loops with a slight increase in the coercive bias values. One would normally expect this shift to be at a minimum due to the relatively symmetric potentials created around the dipole couple. However, the position of the defects with respect to the electrodes and their assigned values already do create a highly asymmetrical distribution of the fields. Moreover, this shift will also depend on the region where the local  $P_x$  value is probed. Thus, we give here the general characteristics and trends to avoid a lengthy discussion on this aspect.

While the loops in the 16 nm IFEC film are displaced along the bias axis with  $p$ -type defects (Fig. 8b), a swelling of these loops accompanies the shifts in the 8 nm film regardless of the presence of bottom electrode (Fig. 8a). One must remember that the  $P_x$  component in the middle of the film is not under the influence of any strong depolarizing or internal bias fields originating from asymmetric boundaries. We note that due to the components of the  $p$ -type defect dipoles along  $+x$  and  $-x$ , the coercive field increases in both signs of the bias axis due to local pinning. In addition, the fields along  $z$ -axis emanating from any inhomogeneity in  $D_z$  in the 8 nm IFEC film are expected to be stronger than in the 16 nm one for the obvious reason: Steeper decay of potentials in the 8 nm film compared to the 16 nm film. The thinner IFEC is more sensitive to  $p$ -type defects as the switching bias for the

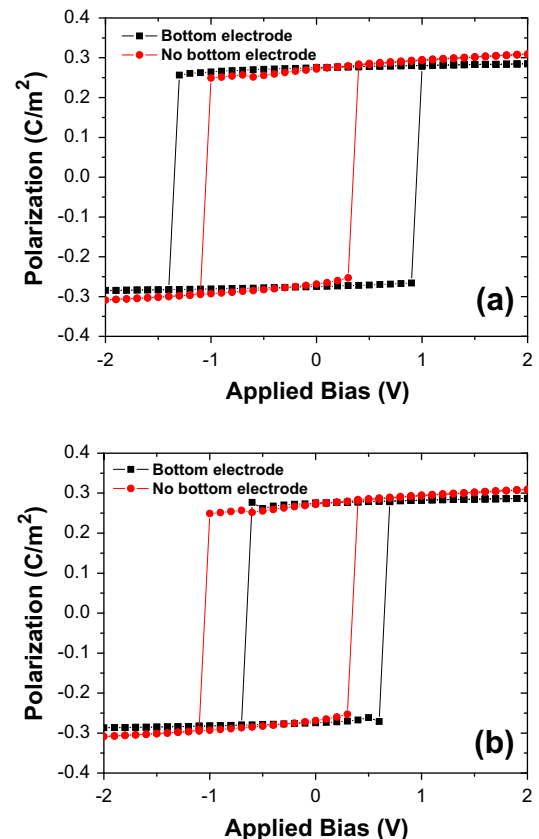


**Fig. 8.** Hysteresis loops and displacement along  $z$  (right axis) for (a) 8 nm thick IFEC film and (b) 16 nm thick IFEC film with polar  $p$ -type defects.

perfect 8 nm and 16 nm thick IFEC structures are nearly the same regardless of the absence or presence of a bottom electrode (Fig. 7).

Overall, despite the complicated nature of the defect effects in the highly inhomogeneous field distribution of the IFEC films, we can make some remarks to a certain extent regarding the hysteresis characteristics: Fig. 8a clearly reveals that the 8 nm IFEC films with defects require higher bias fields to switch  $P$  in between the electrodes. The bottom electrode strongly alters the switching characteristics of the system and the way in which the loops shift are relatively different in the 8 nm and 16 nm thick IFEC films. The 8 nm thick IFEC system suffers more profoundly from pinning due to defects. A striking characteristic, however, to note in both the 8 nm and 16 nm IFEC films is that there is nearly no deformation of loops and they preserve the squareness. The absence of a bottom electrode apparently eradicates easy switching in the 16 nm film with defects but no such conclusion can be arrived at for the 8 nm thick IFEC film. With efficient IC architecture, IFECs might be a feasible option to tailor owing to the nearly defect insensitive nature of the  $P_x$  remanence.

#### 4. Conclusions

In this study, we showed that due to the configuration of  $P$  in IFEC type capacitors, the sensitivity of these systems to electrostatic BCs is dramatically less than SC type. The IFEC switching is impacted by the presence or absence of a bottom electrode, implying the coupling of  $P_x$  to induced  $P_z$  near switching. Our simulations indicate that  $D_z$  makes a sharp anomaly at the coercive field of the  $P_x$  and can be used as a signal to sense switching. This signal, however, nearly disappears when a bottom electrode is not present and concomitantly thermodynamic coercive fields for  $P_x$  increases.

The presence of  $p$ -type polar in IFEC films induces a shift in the loops along the bias axis, accompanied by an increase in the coercive fields for ultrathin structures. The overall effect of frozen-in dipolar  $p$ -type defects is that the steep gradients around the defect sites that decay towards the electrodes create strongly inhomogeneous fields. These fields, in the case of the SC type films, strongly couple to  $P_z$ , a well understood and natural outcome, while the coupling of these fields in the IFEC geometry to  $P_x$  is weaker. The polar defects in thin IFEC films increase the coercive bias in the thermodynamic limit due to spatial pinning but no loss of remanency due to electrical domain formation following removal of the bias is observed. A continuous distribution of space charge when relatively high in density, on the other hand, destroys any remanence in IFEC structures after removal of bias and nearly no hysteresis is ex-

pected, a profound difference compared to the effect of polar defects. The impact of space charges on phase transition and retention characteristics of ultrathin structures, in our view, deserve separate attention and will be given in another study.

#### References

- [1] Dawber M, Rabe KM, Scott JF. *Rev Mod Phys* 2005;77:1083.
- [2] Mehta RR, Silverman BD, Jacobs JT. *J Appl Phys* 1973;44:3379.
- [3] Bratkovsky AM, Levanyuk AP. *Phys Rev Lett* 2000;84:3177.
- [4] Shaw TM, Troiler-Mckinstry S, Mcintyre PC. *Ann Rev Mater Sci* 2000;30:263.
- [5] Junquero J, Ghosez P. *Nature* 2003;422:506.
- [6] Gerra G, Tagantsev AK, Setter N, Parlinski K. *Phys Rev Lett* 2006;96:107603.
- [7] Gerra G, Tagantsev AK, Setter N. *Phys Rev Lett* 2007;98:207601.
- [8] Massimiliano Stengel, Spaldin Nicola A. *Nat Lett* 2006;443:679.
- [9] Yacoby Y, Girshberg Y, Stern EA, Clarke R. *Phys Rev B* 2006;74:104113.
- [10] Prosandeev S, Bellaiche L. *Phys Rev B* 2007;75:172109.
- [11] Zhou C, Newns DM. *J Appl Phys* 1997;82:3081.
- [12] Ahluwalia R, Srolovitz DJ. *Phys Rev B* 2007;76:174121.
- [13] Hu SY, Li YL, Chen LQ. *J Appl Phys* 2003;94:2542.
- [14] Nagarajan V, Jia CL, Kohlstedt H, Waser R, Misirlioglu IB, Alpay SP, et al. *Appl Phys Lett* 2004;86:192910.
- [15] Li YL, Hu SY, Choudhury S, Baskes MI, Saxena A, Lookman T, et al. *J Appl Phys* 2008;104:104110.
- [16] Wang Y, Niranjana MK, Janicka K, Velez JP, Zhuravlev MYe, Jaswal SS, et al. *Phys Rev B* 2010;82:094114.
- [17] Xiao Y, Shenoy VB, Bhattacharya K. *Phys Rev Lett* 2005;95:247603.
- [18] Zhang Y, Li J, Fang D. *Phys Rev B* 2010;82:064103.
- [19] Hong L, Soh AK, Du QG, Li JY. *Phys Rev B* 2008;77:094104.
- [20] Xu B, Cross LE, Bernstein JJ. *Thin Solid Films* 2000;712:377–8.
- [21] Haeni JH, Irvin P, Chang W, Uecker R, Reiche P, Li YL, et al. *Nature* 2004;430:758.
- [22] Dayal K, Bhattacharya K. *Acta Mater* 2007;55:1907.
- [23] Xu B, Polcawich RG, Troiler-Mckinstry S, Ye Y, Cross LE. *Appl Phys Lett* 1999;75:4180.
- [24] El-Naggar MY, Dayal K, Goodwin DG, Bhattacharya K. *J Appl Phys* 2006;100:114115.
- [25] Torii K, Colla EL, Song HW, Tagantsev AK, No K, Setter N. *Integ Ferro* 2001;32:907.
- [26] Zhou Q, Zhang Q, Xu B, Troiler-Mckinstry S. *J Am Ceram Soc* 2002;85:1997.
- [27] Rivkin TV, Carlson CM, Parilla PA, Ginley DS. *Integ Ferro* 2000;29:215.
- [28] Pertsev NA, Zembilgotov AG, Tagantsev AK. *Phys Rev Lett* 1998;80:1988.
- [29] Levanyuk AP, Sigov AS. Defects and structural phase transitions. In: Taylor W, editor. *Ferroelectricity and related phenomena*, vol. 6. Gordon and Breach; 1988.
- [30] Pöykkö S, Chadi DJ. *Phys Rev Lett* 1999;83:1231.
- [31] Cockayne E, Burton BP. *Phys Rev B* 2004;69:144116.
- [32] Bratkovsky AM, Levanyuk AP. *Phys Rev B* 2000;61:15042.
- [33] Morozovska AN, Eliseev EA. *J Phys Condens Mater* 2004;16:8937.
- [34] Pintilie L, Alexe M. *J Appl Phys* 2005;98:123103.
- [35] Zubko P, Jung DJ, Scott JF. *J Appl Phys* 2006;100:114112.
- [36] Misirlioglu IB, Alexe M, Pintilie L, Hesse D. *Appl Phys Lett* 2007;91:022911.
- [37] Okatan MB, Alpay SP. *Appl Phys Lett* 2009;95:092902.
- [38] Okatan MB, Mantese JV, Alpay SP. *Acta Mater* 2010;58:39.
- [39] Anbusathaiah V, Nagarajan V, Aggarwal S. *Appl Phys Lett* 2006;89:132912.